J Mater Sci: Mater Electron (2024) 35:1137

The electrical and dielectric features of Al/$YbFeO_3$/*p*-Si/Al and Al/$YbFe_{0.90}Co_{0.10}O_3$/*p*-Si/Al structures with interfacial perovskite-oxide layer depending on bias voltage and frequency

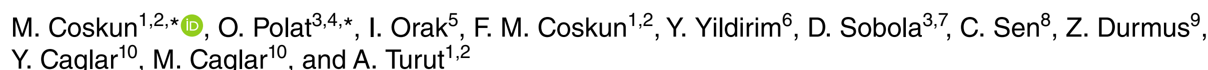

M. Coskun[1,2,*], O. Polat[3,4,*], I. Orak[5], F. M. Coskun[1,2], Y. Yildirim[6], D. Sobola[3,7], C. Sen[8], Z. Durmus[9], Y. Caglar[10], M. Caglar[10], and A. Turut[1,2]

[1] *Department of Engineering Physics, Faculty of Engineering and Natural Sciences, Istanbul Medeniyet University, Uskudar, 34700 Istanbul, Türkiye*
[2] *Istanbul Medeniyet University Science and Advanced Technology Research Center (IMU-BILTAM), Istanbul, Türkiye*
[3] *CEITEC BUT, Brno University of Technology, Purkyňova 123, 612 00 Brno, Czech Republic*
[4] *Tallinn European School, Tehnika 18, 10149 Tallinn, Estonia*
[5] *Vocational School of Health Services, Bingol University, 12000 Bingol, Türkiye*
[6] *Department of Mechanical Engineering, Faculty of Engineering and Natural Sciences, Istanbul Bilgi University, Eyüpsultan, 34060 Istanbul, Türkiye*
[7] *Institute of Physics of Materials, Academy of Sciences of the Czech Republic, Žižkova 22, 616 62 Brno, Czech Republic*
[8] *Department of Physics, Lamar University, Beaumont, TX 77710, USA*
[9] *Department of Biomedical Engineering, Faculty of Engineering and Natural Sciences, Biruni University, 34010 Istanbul, Türkiye*
[10] *Department of Physics, Faculty of Science, Eskisehir Technical University, Yunusemre Campus, 26470 Eskisehir, Türkiye*

Received: 17 April 2024
Accepted: 1 June 2024
Published online: 14 June 2024

© The Author(s), 2024

ABSTRACT

In this investigation, thin films of $YbFeO_3$, both in its pure form and doped with 10% Co, were fabricated on a *p*-Si substrate at 500 °C through the radio-frequency magnetron sputtering method. Examination via Scanning Electron Microscopy demonstrated a porous texture for the pure sample, contrasting with a smooth and crack-free surface post-Co doping. Analysis via X-ray photoelectron spectroscopy unveiled Yb's 3 + oxidation state, alongside the presence of lattice oxygen, oxygen vacancies, and adsorbed oxygen evident in Gaussian fitting curves. Photoluminescence spectroscopy revealed an augmented emission intensity, likely attributed to increased defect initiation in the Co-doped specimen. Moreover, Raman spectroscopy was employed to identify vibration modes in the examined samples, demonstrating shifts in Raman peaks indicative of Co substitution and subsequent distortion in the crystal structure of $YbFeO_3$. Electrical assessments were conducted at room temperature (300 K) under ambient conditions, employing voltage and frequency as variables. Capacitance–voltage measurements illustrated the emergence of an accumulation, with depletion and inversion regions

Address correspondence to E-mail: mustafa.coskun@medeniyet.edu.tr; ozgurpolat7@gmail.com

https://doi.org/10.1007/s10854-024-12896-8

manifesting at different frequencies based on the applied voltage, attributed to the $YbFeO_3$ interfacial layer at the Al and *p*-Si interface. The conductance-voltage characteristics indicated that the structure exhibited maximum conductance in the accumulation region. Series resistance for these configurations was deduced from capacitance-conductance-voltage measurements, indicating a dependence on both bias voltage and frequency. The doping process led to a reduction in capacitance and series resistance, accompanied by an increase in conductance values. After obtaining corrected capacitance and conductance parameters, it became evident that series resistance significantly influences both parameters. Interface state density (N_{ss}), determined through the Hill-Coleman relation demonstrated a decreasing trend with increasing frequency. The pure sample exhibited higher interface state density compared to the Co-doped sample at each frequency, highlighting that the 10% Co-doped $YbFeO_3$ thin film enhances the quality of the metal–semiconductor interface properties compared to the pure contact.

1 Introduction

Measurements of electrical and dielectric properties of novel materials are vital in identifying their potential use in electronic device applications. Among those materials, metal-oxides [1], composites [2], polymers [3], perovskite-oxides [4], and organics [5] are studied extensively in the literature. Perovskite-oxides, which have the ABO_3 chemical formula, are one of the most worthy material classes for scientists due to their unique electrical, optical, magnetic, etc. properties [6–8]. Since these properties can be controlled or modified via doping a foreign element into the A or B site, researchers have intensely studied perovskite-oxides materials recently [6–8]. A member of the perovskite-oxide compound family, the rare earth orthoferrites ($RFeO_3$, *R* denotes as rare earth element), have also been studied highly due to their unique electrical/dielectric, magnetic, and optical properties [9–11]. Ytterbium iron oxide, $YbFeO_3$, is an important rare earth orthoferrite with an optical band gap of around 2.1 eV [12]. In its powdered form, $YbFeO_3$ adopts an orthorhombic crystalline structure, while in thin film form, depending on the substrate temperature [13], it can manifest in orthorhombic and/or hexagonal crystalline structures [14]. $YbFeO_3$, owing to its multiferroic characteristics, finds diverse applications ranging from solar cells to magnetoelectric couplers, gas sensors, and photo-catalysts [15–19]. Previous research has predominantly concentrated on the magnetic aspects of $YbFeO_3$ in thin film form, primarily due to the magnetic properties of the iron (Fe) ion [14, 20]. In contrast, the literature on the electrical and dielectric properties of $YbFeO_3$ remains relatively limited. Our research group has previously investigated the optical band gap engineering and crystalline structure of thin film $YbFeO_3$ compounds with various doping ratios [12, 21, 22]. Additionally, the current–voltage characteristics and current transport mechanism of $YbFeO_3$ thin films have been explored in prior publications [23]. Notably, there is a lack of existing literature on the study of electrical properties for both pure and cobalt (Co)-doped $YbFeO_3$ thin films. This research aims to address this gap and contribute valuable insights into the electrical properties of thin film $YbFeO_3$, providing essential knowledge for researchers in the field. Researchers have extensively investigated the electrical and dielectric properties of metal-interface layer-semiconductor devices [24]. This method involves placing an insulator or semiconductor material between a metal–semiconductor interface to create a capacitor-like device using various thin film growth techniques [25–29]. Such circuit elements serve as fundamental components in many electronic devices, particularly in controlling the performance of diodes and field-effect transistors [30]. Parameters like interface states, series resistance, and barrier height play crucial roles in the functionality of semiconductor electronic devices [30, 31]. To introduce new materials for high-performance electronic

device applications, researchers have explored numerous compounds [32–34]. However, detailed studies on the electrical and dielectric properties of pure and Co-doped $YbFeO_3$ thin films are lacking in the existing literature.

In this research, we deposited thin films of both undoped and 10% cobalt (Co)-doped $YbFeO_3$ on a *p*-Si substrate using the radio frequency sputtering technique. Scanning electron microscopy (SEM) images were scrutinized to analyze the morphology of the specimens. Furthermore, X-ray photoelectron spectroscopy (XPS), photoluminescence (PL), and Raman Spectra analyses were conducted to investigate the chemical properties of the samples under study. To construct the Al/$YbFeO_3$/*p*-Si structure, a metal electrode was deposited on both sides (front and back) of the devices. Electrical properties were evaluated under ambient conditions at room temperature. Capacitance (C), conductance (G), series resistance (R_s), impedance (Z), and interface states (N_{ss}) of the devices were examined by varying the bias voltage at different frequency settings.

2 Experimental

In this section, 2-inch diameter sputter targets were prepared through manual pressing with a 400-bar pressure application. To achieve this, the $YbFeO_3$ powder was synthesized using a solid-state reaction procedure, employing Yb_2O_3 (ABCR) and Fe_2O_3 (Sigma-Aldrich) samples with purities exceeding 99.9% and more than 99%, respectively. These powders were blended to the desired stoichiometry in an agate mortar and immersed in ethanol solvent for over an hour. The resulting powder underwent calcination at 900 °C for 10 h in ambient conditions. Following the initial calcination, the powder was reground to ensure homogeneity in the agate mortar, then sintered at 1200 °C for 12 h under ambient conditions. Finally, the powder was pressed as described above, resulting in the desired $YbFeO_3$ sputter target. The same steps were followed for the 10% Co-doped $YbFeO_3$ ($YbFe_{0.90}Co_{0.10}O_3$) powders and targets, using 99.7% pure Co_3O_4 powders from A. AESAR. These targets were employed as magnetron sputter targets in the physical vapor deposition (PVD) system.

For the chemical cleaning process, the *p*-Si type substrate (1–10 Ω cm resistivity, (100) oriented and boron-doped) underwent exposure to acetone, isopropyl alcohol (IPA), and de-ionized water. Subsequently, approximately 100 nm thick aluminum (Al) was thermally evaporated onto the Si's rough surface. To facilitate electron transfer between Al and Si and achieve ohmic contact, the coated substrate was annealed at around 550 °C for 5 min under nitrogen gas flow.

In the thin film growth process on the bright side, the substrate was transferred to a vacuum chamber, which was pumped until the pressure reached around 10^{-7} mTorr. Pure and Co-doped $YbFeO_3$ thin films were produced through rf sputtering (100 watts) at a 2.5 mTorr chamber pressure and 20 sccm argon (Ar) gas flow concentration, with the substrate heated at 500 °C and periodically rotated for approximately 2 h. After completing the depositions, pure and 10% Co-doped $YbFeO_3$ thin films with thicknesses of 205 and 615 nm were obtained. The oxidation states of the elements were determined through X-ray photoelectron spectroscopy (XPS) measurements. The C 1s peak at 284.6 eV was utilized for calibration. Photoluminescence (PL) experiments were conducted on a micro-Raman spectroscope alpha 300R (Witec) using a 355 nm excitation laser with 0.5 mW intensity. Raman analyses were carried out using a 532 nm excitation laser with 20 mW power (Zeiss EC).

Finally, to form a rectifying contact, high-purity Al (99.999%) was evaporated onto the top side of the $YbFeO_3$/*p*-Si/Al structure, resulting in the desired structure. The electrical properties of the Al-coated $YbFeO_3$ structure were investigated in ambient conditions using a source meter (Keithley 2400) and an Impedance Analyzer (HP4192 A LF). The results are discussed in the subsequent section.

3 Results and discussion

Figure 1a displays the SEM image of the pure $YbFeO_3$ sample, revealing the presence of a spongy surface. Upon undergoing the doping process, this spongy surface diminishes, giving way to a dense and crack-free surface as depicted in Fig. 1b. The smooth surface texture seen in samples doped with cobalt could be linked to the decrease in lattice parameters of $YbFeO_3$ induced by cobalt doping. In our prior research, we noted that introducing Co into Fe positions within $YbFeO_3$ resulted in a decrease in lattice parameters [35]. Nforna et al. similarly observed a reduction in lattice parameters in $NdFeO_3$ when Co was substituted into Fe sites [36]. They suggested that this decrease in

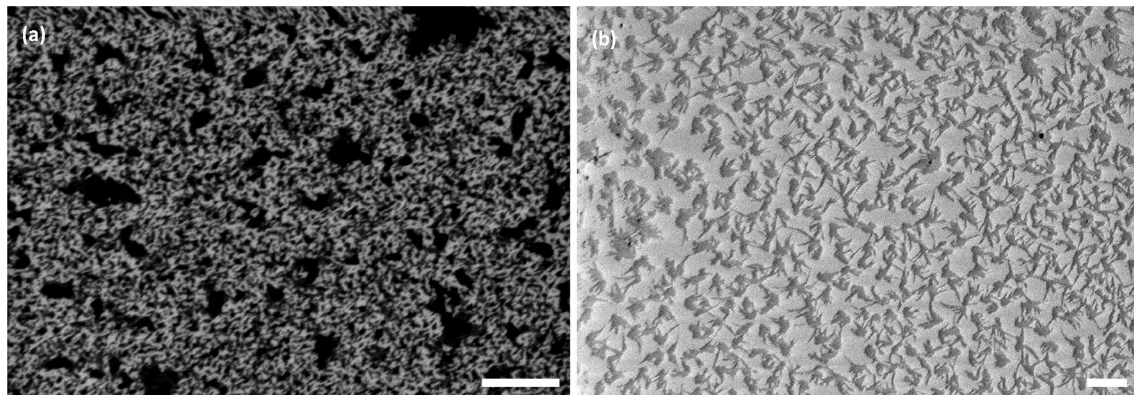

Fig. 1 **a** SEM image of pure and **b** 10% Co-doped $YbFeO_3$ thin films (Scale bars show 2 µm)

lattice parameters and unit cell volume led to a more compact and uniform crystal structure. Additionally, Bai et al. demonstrated that Co-doped $BiFeO_3$ thin films exhibited uniformly dense surfaces and a homogeneous surface morphology [37]. They attributed these characteristics to the smaller size of Co ions.

In our prior investigation [12], we conducted X-ray diffraction studies on both pure and Co-doped $YbFeO_3$ compounds. It was observed that both types of compounds exhibit a polycrystalline crystal structure (without any other phases), with the Co-doping process leading to an increase in crystallite size [12]. The XPS analysis of the studied thin films is illustrated in Fig. 2. The full spectrum, represented in Fig. 2a, depicts the binding energy's dependency. Figure 2b illustrates the Yb 4d spectrum for both thin films, indicating binding energies of approximately 184.86 eV and 184.44 eV for the $4d_{5/2}$ configuration, and around 199 eV and 198.61 eV for the $4d_{3/2}$ configuration, for undoped and 10% Co-doped $YbFeO_3$ thin films, respectively. These obtained binding energies imply a Yb oxidation state of 3 + [38]. In Fig. 2c and d, the oxygen (O) 1s spectrum for undoped and 10% Co-doped $YbFeO_3$ thin films is displayed. The Gaussian fitting reveals that the undoped $YbFeO_3$ exhibits two distinct peaks, while the 10% Co-doped sample displays three peaks [39]. In the undoped sample, the peak at 529.80 eV originates from lattice oxygen, and the peak at 532 eV arises from oxygen vacancies and defects [39]. Conversely, the 10% Co-doped sample presents peaks at 527.37, 529.52 eV, and 531.84 eV, respectively. The first peak may be attributed to O^{2-} ions absorbed on the thin film surface [39], the second to lattice oxygens [39], and the third to oxygen vacancies and defects [39]. Fe and Co XPS analyses were previously conducted in our study, revealing that pure $YbFeO_3$ contains both Fe^{2+} and Fe^{3+} ions, while the 10% Co-doped $YbFeO_3$ compound consists solely of Fe^{3+} ions [12].

Moreover, XPS analysis indicates that the 10% Co-doped $YbFeO_3$ compound comprises both Co^{2+} and Co^{3+} ions [12]. AFM analysis was conducted for the mentioned compounds, revealing that the pure compound has a roughness of 2.57 nm, while the 10% Co-doped $YbFeO_3$ compound exhibits a roughness of 1.86 nm [12]. Furthermore, we investigated the optical band gaps of the pure and Co-doped $YbFeO_3$ compounds, revealing values of 2.10 eV and 1.72 eV for the pure and 10% Co-doped $YbFeO_3$ compounds, respectively [12]. The decrease can be ascribed to two main factors: (i) the formation of more defects such as oxygen vacancies within the material and (ii) the differences in electronegativity between B cations and oxygen [12].

Photoluminescence (PL) spectroscopy serves as a valuable method for examining the recombination of photogenerated electron–hole pairs within materials. Figure 3 illustrates the PL spectra of the pure and 10% Co-doped $YbFeO_3$ thin films. As depicted in the plots, the emission intensity increases following the doping process, possibly due to heightened levels of defect formation post-doping [40]. These defects can capture or trap electrons within the materials.

Figure 4 displays the Raman spectra for undoped and 10% Co-doped $YbFeO_3$ thin films. The acquired peaks largely remain consistent, except for the peak around 600 cm^{-1}, which arises from the Co-doping into the parent compound. Peaks below 200 cm^{-1} are attributed to the vibration of heavy rare-earth ions present in the sample [41]. The harmonic oscillator frequency,

Fig. 2 XPS analysis of undoped and 10% Co-doped $YbFeO_3$ thin films. **a** Full spectrum, **b** Yb 4 days, O 1s spectrum of **c** undoped, and **d** 10% Co-doped $YbFeO_3$ thin films, respectively

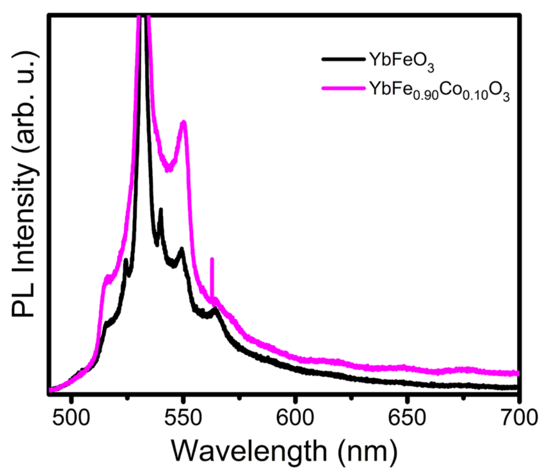

Fig. 3 Photoluminescence (PL) analysis of the $YbFeO_3$ and $YbFe_{0.90}Co_{0.10}O_3$ thin films

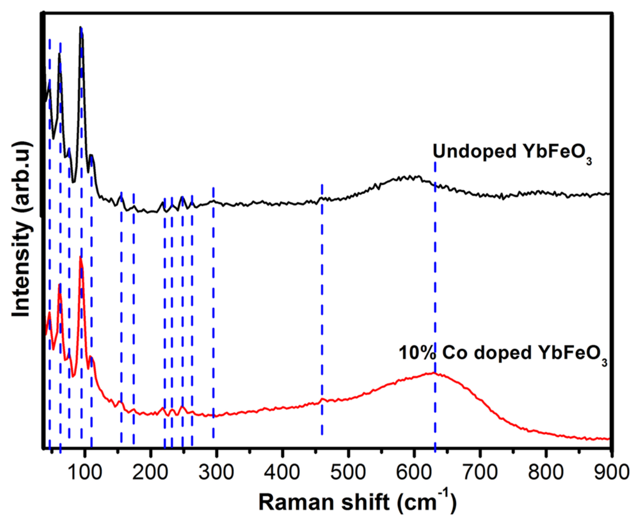

Fig. 4 Raman spectra for undoped and 10% Co-doped $YbFeO_3$ thin films

ω, is proportional to ω ~ $(k/M)^{1/2}$, where k and M represent the spring constant and atomic mass, respectively. From this relationship, it can be inferred that heavy ions exhibit lower vibration frequencies [41].

Peaks within the range of 200–350 cm^{-1} are primarily associated with FeO_6 octahedral tilting, while the peak at approximately 460 cm^{-1} originates from the excitation of Fe^{3+} magnetic ions [41]. Peaks beyond 500 cm^{-1} predominantly stem from Fe–O stretching vibrations [41, 42]. Notably, peaks around 630 cm^{-1} are attributed to the Fe–O bond. Furthermore, it's observed that the doping process can induce spectrum shifts, which may be attributed to crystal distortion or structural disorder resulting from Co-doping into the parent compound.

Figure 5 a shows the energy-band diagram of the $YbFeO_3$/*p*-Si heterojunction before the contact. Here χ, E_C, E_V, E_g, E_F, ΔE_C, and ΔE_V are the electron affinity, conduction band minimum, valance band maximum, optical band gap, Fermi energy level, conduction band difference, and valance band difference between the $YbFeO_3$ and Si, respectively.

The energy band diagram for the $YbFeO_3$ is provided in Refs. [12, 15]. According to Ref. [15], the energy difference between the conductance band minimum of Si and $YbFeO_3$ is $\Delta E_C = 0.45$ eV, the valance band maximum is $\Delta E_V = 0.53$ eV, and the electron affinity of $YbFeO_3$, χ_{YbFO} is around 3.6 eV. The optical band gap of $YbFeO_3$ was given in our previous study and the detailed data was presented in the mentioned study [12]. Figure 5b shows the schematic illustration of the studied structure.

Figure 6 illustrates the capacitance–voltage (*C-V*) characteristics for both the undoped $YbFeO_3$/*p*-Si and 10% Co-doped $YbFeO_3$/*p*-Si samples across various frequency values. In Fig. 6a, the undoped sample exhibits maximal capacitance values in the positive bias region applied to the ohmic back electrode of the Si wafer

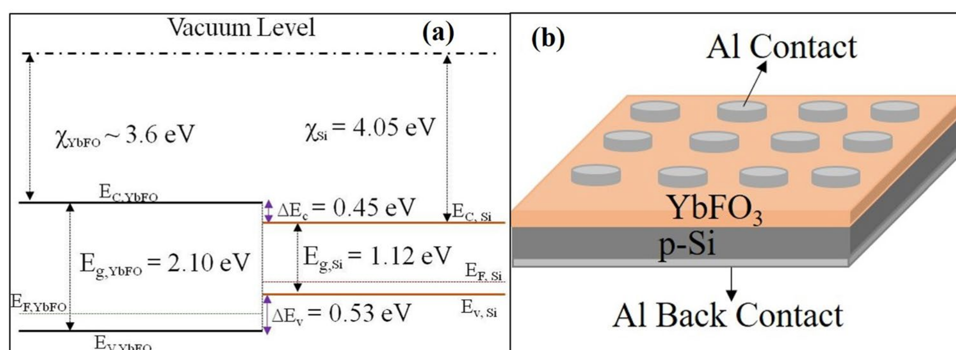

Fig. 5 **a** Energy-band diagram of $YbFeO_3$/*p*-Si heterojunction, **b** schematic illustration of Al/$YbFeO_3$/*p*-Si device

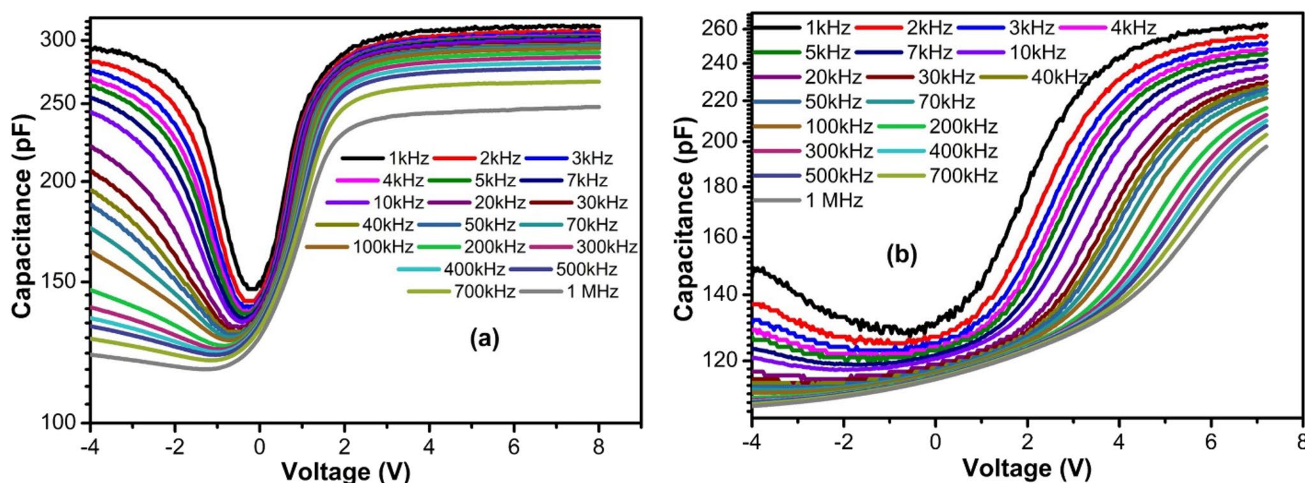

Fig. 6 The capacitance–voltage (*C-V*) characteristic for **a** the undoped device, and **b** the 10% Co-doped $YbFeO_3$ device at various frequency values

(with a negative bias applied to the $YbFeO_3$ contact) at lower frequency values. This region, known as the accumulation region, witnesses the accumulation of all majority carriers (holes) in the *p*-type silicon on the surface of the Si adjacent to the $YbFeO_3$ thin film. The Coulomb interaction causes these holes to induce negative charge accumulation in the $YbFeO_3$ thin film near the $YbFeO_3$/*p*-Si interface. As the applied positive bias decreases or sweeps through zero, the capacitance value begins to decrease to a minimum value, marking the depletion region, which acts as a dielectric in series with the semiconductor. Subsequently, the capacitance increases with increasing negative applied bias voltage at relatively lower frequency regions. The capacitance value at negative applied bias, applied to the back of the Si wafer (with a positive bias applied to the $YbFeO_3$ contact), denotes the inversion region capacitance value. At lower frequency regions, the capacitance almost matches the accumulation capacitance value due to the minority charge contribution in the inversion region. In the inversion region at lower frequencies, the minority carriers can trail the external electrical field, influencing the capacitance value of the device. However, at higher frequencies, the minority carriers fail to track the external electrical field, resulting in decreased capacitance value in this region.

In the accumulation region, it is evident that the capacitance declines with increasing frequency, indicating the presence of interface states that affect the capacitance value of the device. The capacitance value in the accumulation region is approximately 313 pF at 1 kHz and 248 pF at 1.0 MHz at 8.0 V for the undoped device. Figure 6b displays the capacitance variations of the 10% Co-doped device at various frequencies. The accumulation region forms at high positive bias values and transitions through zero bias value, where the depletion region becomes apparent. The inversion region is distinctly observable at negative bias values. The capacitance value decreases post-doping process, with a value of around 293 pF at 1 kHz and 197 pF at 1 MHz at 7.0 V for the 10% Co-doped device. This reduction in capacitance value in the 10% Co-doped sample might be ascribed to the formation of defects, as indicated in our PL study. These defects may impede the movement of charge carriers or serve as trap centers for them, thereby reducing the effective number of charges that can be stored in our sample. The capacitance difference (between low and high frequency) is notably higher than that of the undoped sample.

The total capacitance (C) of the device is a combination of both oxide (C_{ox}) and the depletion layer capacitance of the silicon (C_D) in high frequency, which are connected in series with each other. Hence, the total capacitance at high frequency can be expressed as [43].

$$\frac{1}{C} = \frac{1}{C_{ox}} + \frac{1}{C_D} \tag{1}$$

In the accumulation region, the majority carriers gather near the $YbFeO_3$/*p*-Si interface, while the depletion capacitance becomes negligible due to the formation of the depletion region. Consequently, the total capacitance is nearly equivalent to the oxide capacitance in this scenario. Specifically, at 7.0 V, the total capacitance measures 312 pF at 1.0 kHz and 246 pF at 1.0 MHz for the undoped compound, and 262 pF at 1.0 kHz and 195 pF at 1.0 MHz for the 10% Co-doped sample. However, in the depletion region, the total capacitance diminishes to a minimum value. Here, the total capacitance combines both oxide and depletion capacitance, linked in series. Consequently, the total capacitance should be lower than the oxide capacitance. Utilizing Eq. (1), the depletion capacitance of both undoped and doped samples can be computed at high frequencies (1.0 MHz). For the undoped device, the depletion capacitance is 223 pF at − 1.0 V, and for the 10% Co-doped device, it measures 242 pF at − 4.0 V. The depletion region width is calculated as 1.12 μm for the undoped device at − 1 V and 1.03 μm for the doped device at − 4.0 V using the following equation:

$$C_D = \frac{\varepsilon_S A}{d}, \varepsilon_S = k\varepsilon_0, \tag{2}$$

where ϵ_0, $k = 11.7 \mathrm{for} Si$, A, and d are the dielectric permittivity of vacuum and dielectric constant of Si, diode area, and depletion region width, respectively.

Figure 1S, in the supplementary section, shows the variation of the dielectric constant (ε′) of the $YbFeO_3$/*p*-Si and 10% Co-doped $YbFeO_3$/*p*-Si devices with voltage at various frequencies, respectively. To calculate the dielectric constant of the devices, the following relation is mainly used:

$$C = \varepsilon' \varepsilon_0 \frac{A}{t_{ox}},\ C_0 = \varepsilon_0 \frac{A}{t_{ox}},\ \varepsilon' = \frac{C}{C_0} \tag{3}$$

Here, C, C_0, ε_0, A, and t_{ox} are the measured capacitance and empty capacitance of the sample, dielectric permittivity of the free space, diode area, and

thickness of the interfacial thin film, respectively. The dielectric constant was measured as 3 at 1.0 kHz and 2.4 at 1.0 MHz for the pure $YbFeO_3$ sample at 7.0 V. The 10% Co-doped $YbFeO_3$ compound has dielectric constants of 7.5 at 1.0 kHz and 5.6 at 1.0 MHz at 7.0 V. The obtained results show that the doping process has a clear effect on the dielectric constant of the $YbFeO_3$ material. In our previous study [35], we examined the role of Co-doping on the $YbFeO_3$ powder compound, and the results showed that the dielectric constant increases with increasing doping ratio. In that study [35], this increase was attributed to (i) Co-doping causing charge carrier creation, and (ii) Co-doping into the $YbFeO_3$ causing lattice contraction due to smaller ion doping, thereby decreasing crystalline size leading to an increase in the number of grain boundaries, respectively [35].

The calculated dielectric constant for the pure and 10% Co-doped devices is very low compared to that of the powder $YbFeO_3$ compound. This may be attributed to poor crystallinity, which was observed by another group [44]. Downie et al. synthesized hexagonal $MFeO_3$ (M = Y, Yb, In) powders and investigated their magnetic, electric, and crystalline properties [44]. They obtained a very low dielectric constant, i.e., 5.4 for $YbFeO_3$ at 100 kHz. They attributed this low value to (i) poor sample crystallinity and (ii) very small crystal size (around 10 nm) [44].

Figure 7 shows the C^{-2} behavior of the device as a function of voltage for various frequencies at 300 K. The curves in this plot were obtained from the C–V curves using the following equations [43],

$$C^{-2} = \frac{2(V_0 - V)}{\varepsilon_s \varepsilon_0 q A^2 N_A} \tag{4}$$

$$\frac{d(C^{-2})}{dV} = -\frac{2}{\varepsilon_s \varepsilon_0 q A^2 N_A} \tag{5}$$

where N_A is the free carrier density, V_0 is the intercept of the linear portion of the C^{-2} *vs.* V plot, V is the applied potential, A is the area of each Al dot onto Al/$YbFeO_3$/p-Si/Al, and Al/$YbFe_{0.90}Co_{0.10}O_3$/p-Si/Al thin layer. The ε_s, ε_o, and q are the permittivity of semiconductor and vacuum and electronic charge, respectively. The intercept potential can be written as [45]:

$$V_0 = V_D - \frac{k_B T}{q} \tag{6}$$

where V_D is the diffusion potential, and k_B and T are the Boltzmann constant and the absolute temperature, respectively. The barrier height (φ_B) can be obtained using [45]:

$$\varphi_B = V_D + E_F - \Delta\varphi_B \tag{7}$$

where E_F is the energy difference between the bulk Fermi level and the valance band edge, and the $\Delta\varphi_B$ is the image force barrier lowering, respectively. Those values are obtained using [45]:

$$E_F = \frac{k_B T}{q} ln\left(\frac{N_V}{N_A}\right) \tag{8}$$

In this equation, N_V is the effective density of states in the valance band of p-type Si and obtained using [46]:

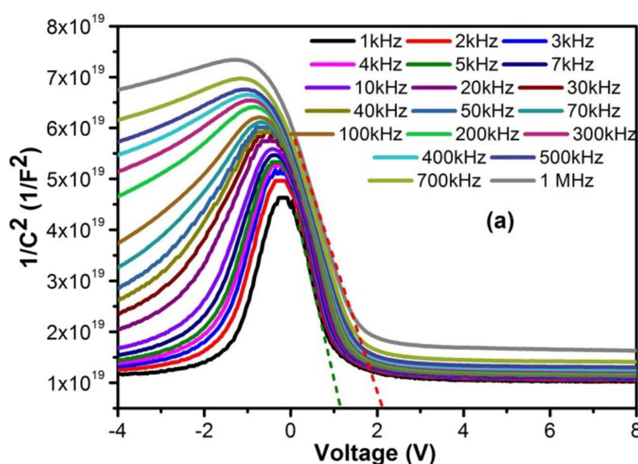

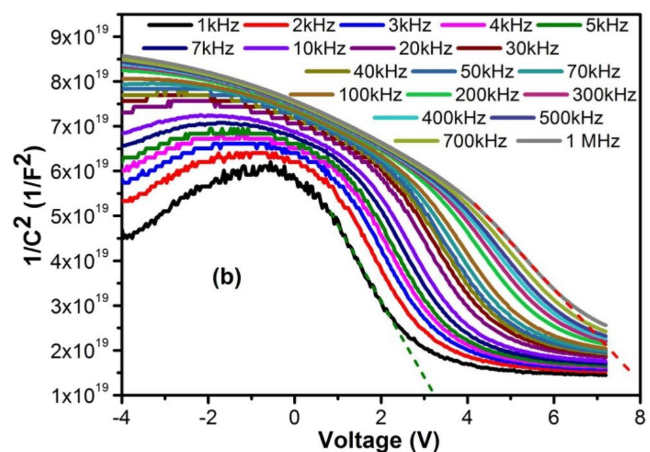

Fig. 7 C^{-2} versus V curves for **a** the pure and **b** 10% Co-doped $YbFeO_3$ devices at a frequency range from 1.0 kHz to 1.0 MHz

$$N_V = 4.82x10^{15}[T]^{3/2}\left[\frac{m_h^*}{m_0}\right]^{3/2} \quad N_V = 1.603x10^{18}\left(cm^{-3}\right)atT = 300K \tag{9}$$

Here the m_h* is the effective mass for holes (m_h* = 0.16m_0) and m_0 is the rest mass of the electron. The image force barrier lowering was obtained using the following equations, in which the E_m is the maximum electrical field [45].

$$\Delta\varphi_B = \sqrt{\frac{qE_m}{4\pi\varepsilon_s\varepsilon_0}} \tag{10}$$

$$E_m = \sqrt{\frac{2qN_AV_0}{\varepsilon_s\varepsilon_0}} \tag{11}$$

All the calculated parameters from the C^{-2} *vs.* V plots for various frequencies are listed in Table 1. It is clear that those parameters strongly depend on frequency and increase with increasing frequency.

The conductance (G) *vs.* voltage (V) dependence for the undoped and doped $YbFeO_3$ devices are shown in Fig. 8a and b. Figure 8a illustrates a maximum in the positive voltage region (or the accumulation region), and a minimum around 0.0 V before increasing slowly in the negative voltage region. It is seen that conductance increases with increasing frequency. This is due to an increase in carrier mobility with increasing frequency. In the accumulation region, the conductance reaches a maximum at a certain voltage and frequency value, and it is clear that the voltage shifts towards higher positive values

Table 1 Calculated parameters from the C^{-2} *vs.* V plots for various frequencies

	$YbFeO_3$							10% Co-Doped $YbFeO_3$						
f (kHz)	V_0 (V)	N_A (cm^{-3})×10^{14}	V_D (V)	E_F (eV)	E_M (V/cm)×10^4	$\Delta\varphi_B$ (eV)	φ_B (eV)	V_0 (V)	N_A (cm^{-3})×10^{15}	V_D (V)	E_F (eV)	E_M (V/cm)×10^4	$\Delta\varphi_B$ (eV)	φ_B (eV)
100	1.82	8.44	1.85	0.196	2.16	0.016	2.03	6.96	1.85	6.99	0.176	6.25	0.027	7.13
200	1.92	8.87	1.95	0.195	2.27	0.017	2.12	7.54	1.98	7.57	0.174	6.73	0.029	7.71
300	1.96	8.99	1.99	0.195	2.31	0.017	2.16	7.85	2.06	7.88	0.173	7.00	0.029	8.02
400	1.98	8.99	2.01	0.195	2.33	0.017	2.18	8.19	2.12	8.22	0.172	7.27	0.030	8.36
500	2.00	8.96	2.03	0.195	2.33	0.017	2.20	8.34	2.18	8.37	0.172	7.43	0.030	8.51
700	2.03	8.93	2.06	0.195	2.35	0.017	2.23	8.67	2.27	8.70	0.171	7.74	0.031	8.84
1000	2.12	8.90	2.15	0.195	2.39	0.017	2.32	9.06	2.38	9.09	0.169	8.09	0.031	9.22

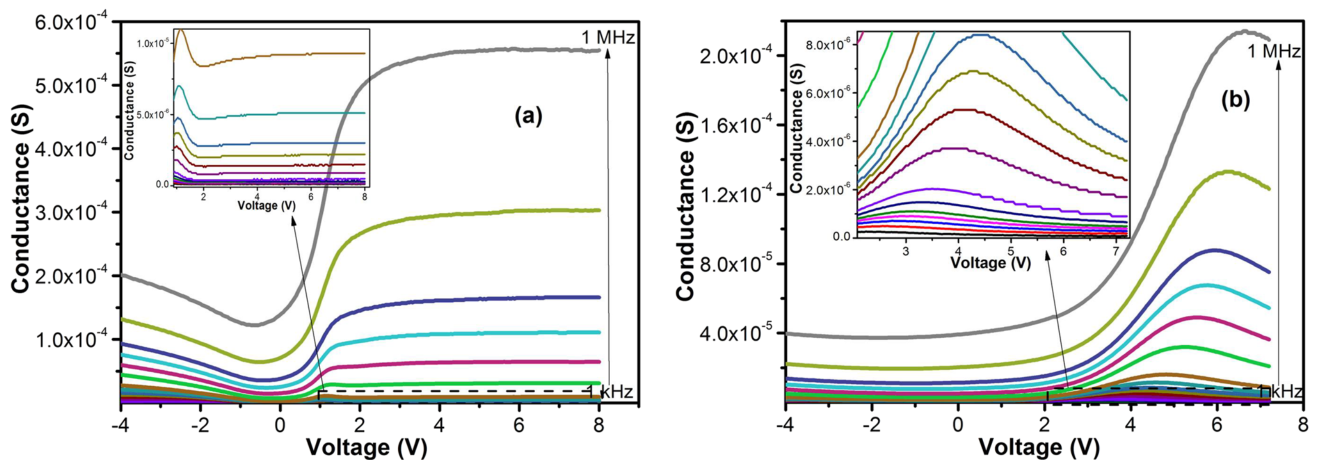

Fig. 8 Conductance (G) *vs.* voltage (V) plots for **a** undoped and **b** 10% Co-doped $YbFeO_3$ devices

with increasing frequency. This is due to interface states and the series resistance effect.

Figures 8a and b depict the dependence of conductance (G) on voltage (V) for both undoped and doped $YbFeO_3$ devices. In Fig. 8a, there is a notable peak in the positive voltage region, corresponding to the accumulation region, with a minimum observed around 0.0 V before gradually increasing in the negative voltage region. Conductance rises with increasing frequency due to enhanced carrier mobility. Within the accumulation region, conductance reaches its maximum at a specific voltage and frequency, with the voltage shifting towards higher positive values as frequency increases. This phenomenon is attributed to interface states and series resistance effects.

At 7.0 V, the conductance value is 1.13×10^{-7} S at 1 kHz and 5.5×10^{-4} S at 1 MHz for the undoped device in the accumulation region. The inset in Fig. 8a displays conductance for suppressed frequency values. The conductance profiles of the 10% Co-doped device are presented in Fig. 8b. It is evident that conductance in the accumulation region advances with increasing positive voltage and frequency values. Peaks in conductance occur at certain voltages for all frequencies in the accumulation region, with these peaks shifting towards higher positive voltages as frequencies increase. This shift is attributed to interface states and series resistance effects. In the negative bias region, conductance remains nearly voltage-independent at given frequencies. The inset of Fig. 8b shows the conductance for suppressed frequency values. Following the doping process, conductance decreases, attributed to lattice distortion acting as a trap site in the device. The role of series resistance is crucial for electronic device performance. Series resistance, R_s, can lead to deviations of parameters such as capacitance and conductance from their ideal values, or it can introduce significant errors during parameter extraction [31].

According to Nicollian and Briews [31], series resistance stems from five distinct sources: (i) the contact established by the probe wire, (ii) the back contact (or ohmic contact) of the substrate, (iii) the quality of the film or any particulate matter situated between two electrodes, (iv) the resistance of the quasi-neutral bulk substrate positioned between the ohmic contact, the substrate, and the depletion layer edge at the substrate surface beneath the gate, and (v) an extremely non-uniform doping distribution of the substrate beneath the gate. These factors significantly influence device performance in potential electronic device applications. Series resistance can be determined through the conductance technique, and according to this method, the series resistance can be calculated using the following equation [31].

$$R_s = \frac{G_m}{G_m^2 + (\omega C_m)^2} \tag{12}$$

where G_m, C_m, and ω are the measured conductance and capacitance, and angular frequency, respectively.

Figure 9a illustrates the behavior of R_s for the undoped device. R_s initially increases up to a certain voltage in the inversion region, then sharply peaks (reaching a maximum value around − 1.0 V) in the depletion region before sharply decreasing. Subsequently, there is an increase of around 0.0 V followed by a second peak, which diminishes with increasing voltage and eventually stabilizes in the high voltage or accumulation region. In the accumulation region, frequency noises are apparent at 1.0 kHz, leading to the removal of data for high voltage values. The noise diminishes at higher frequency values. The observed peak heights decrease with increasing frequency, with clearer peaks evident at lower frequency values. The measured resistance values in the accumulation region are approximately 11.3 kΩ at 2.0 kHz and 211 Ω for the undoped device at 1.0 MHz at 7.0 V. In Fig. 9b, R_s plots for the 10% Co-doped device exhibit a similar behavior to that of the undoped device. Two peaks are noted for low frequencies, while only a single peak is observed at high frequencies. The peak in the positive voltage region shifts towards higher positive values with increasing frequency, attributed to reordering and restructuring under the applied bias at different frequencies. The obtained resistance values are 29.7 kΩ at 2.0 kHz and 158.6 Ω at 1 MHz for the 10% Co-doped sample at the same voltage value (7.0 V). Figure 9c compares the dependence of series resistance on voltage for each device at 1.0 MHz. In the accumulation region, the undoped device shows a decrease in the inversion region before peaking between 1.0 V and 2.0 V, followed by almost voltage-independent behavior between 2.0 V and 7.0 V. The doped device displays a slight decrease in the inversion region before gradually increasing in the depletion region, then sharply increasing around 4.0 V. This increase peaks around 8.0 V and decreases again. The undoped device has lower resistance than the doped one at 1.0 MHz. Figure 9d depicts the dependence of series resistance

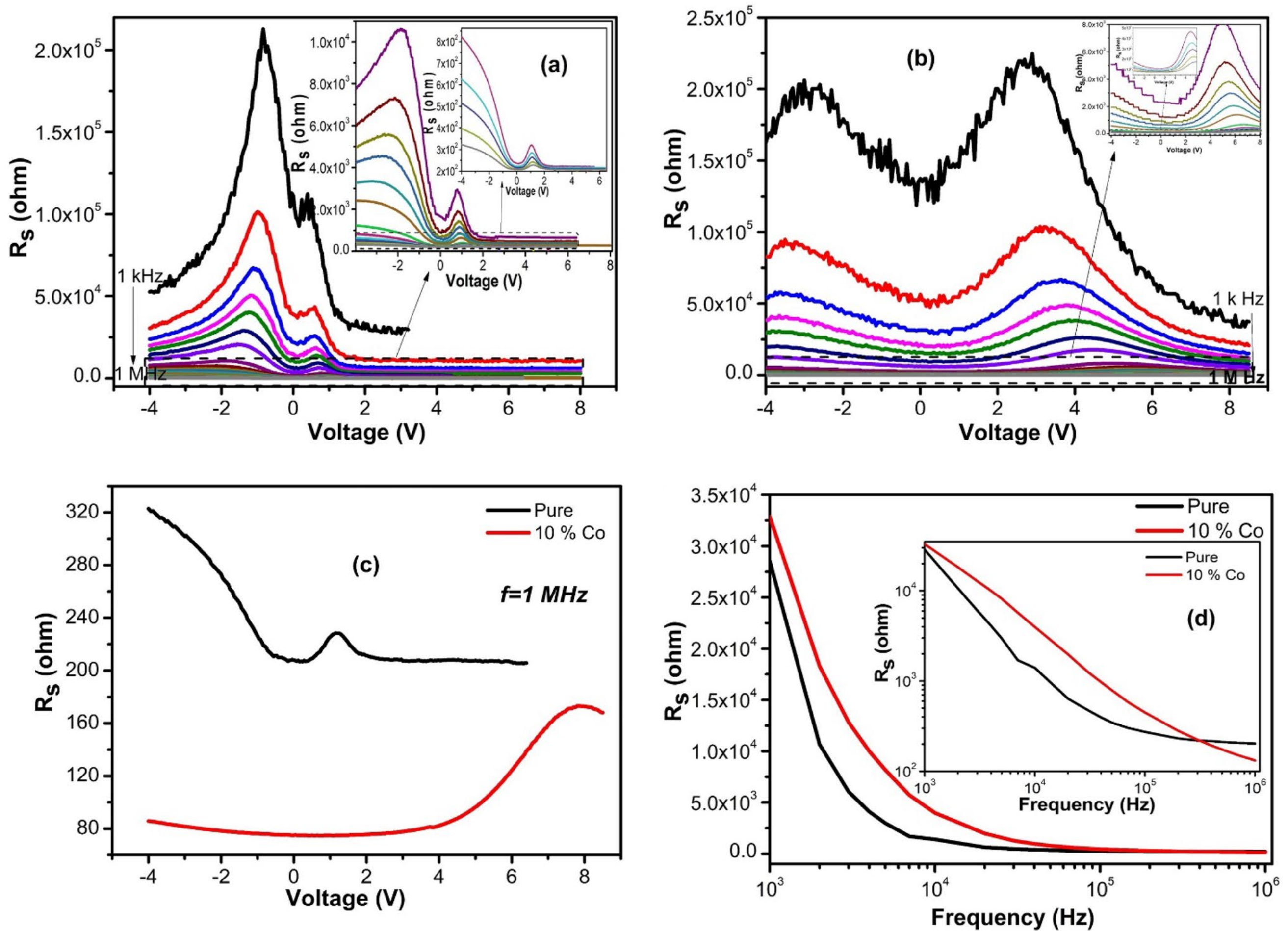

Fig. 9 Series resistance (R_s) of the **a** undoped and **b** 10% Co-doped devices, **c** comparison of the R_s at 1 MHz, and **d** frequency-dependent R_s variation for both devices at 7 V

on frequency in the strong accumulation region (at 7.0 V) for each device. Series resistance decreases with increasing frequency for each device at low frequencies. While this decrease slows down in the middle-frequency region, it remains almost constant in the higher-frequency region. The 10% Co-doped device exhibits higher resistance values between 1.0 kHz and 500 kHz. Beyond 500 kHz, the undoped device has lower resistance than the doped one. The inset is plotted using the log–log scale.

Because of the influence of series resistance, the measured capacitance (C_m) and conductance (G_m) stray from their theoretical values. To rectify these discrepancies and acquire accurate capacitance and conductance values, corrections must be made to these parameters. The adjusted capacitance (C_c) and conductance (G_c) can be determined using the following formulas: [31]:

$$C_c = \frac{\left(G_m^2 + \omega^2 C_m^2\right) C_m}{a^2 + \omega^2 C_m^2} \tag{13}$$

$$G_c = \frac{\left(G_m^2 + \omega^2 C_m^2\right) a}{a^2 + \omega^2 C_m^2} \tag{14}$$

where $a = G_m - \left(G_m^2 + \omega^2 C_m^2\right) R_s$, and the measured capacitance (C_m) and conductance (G_m) are experimental values that come from the *C-V* and *G-V* measurements. Figures 10a and b depict the adjusted capacitance profiles of the pure and 10% Co-doped devices across varying voltage levels at different frequencies. In comparison to the measured capacitance profiles, the corrected capacitance exhibits higher values for both devices. Figures 10c and d present the comparative plots of measured and corrected capacitance for the pure and 10% Co-doped devices at 1.0 MHz,

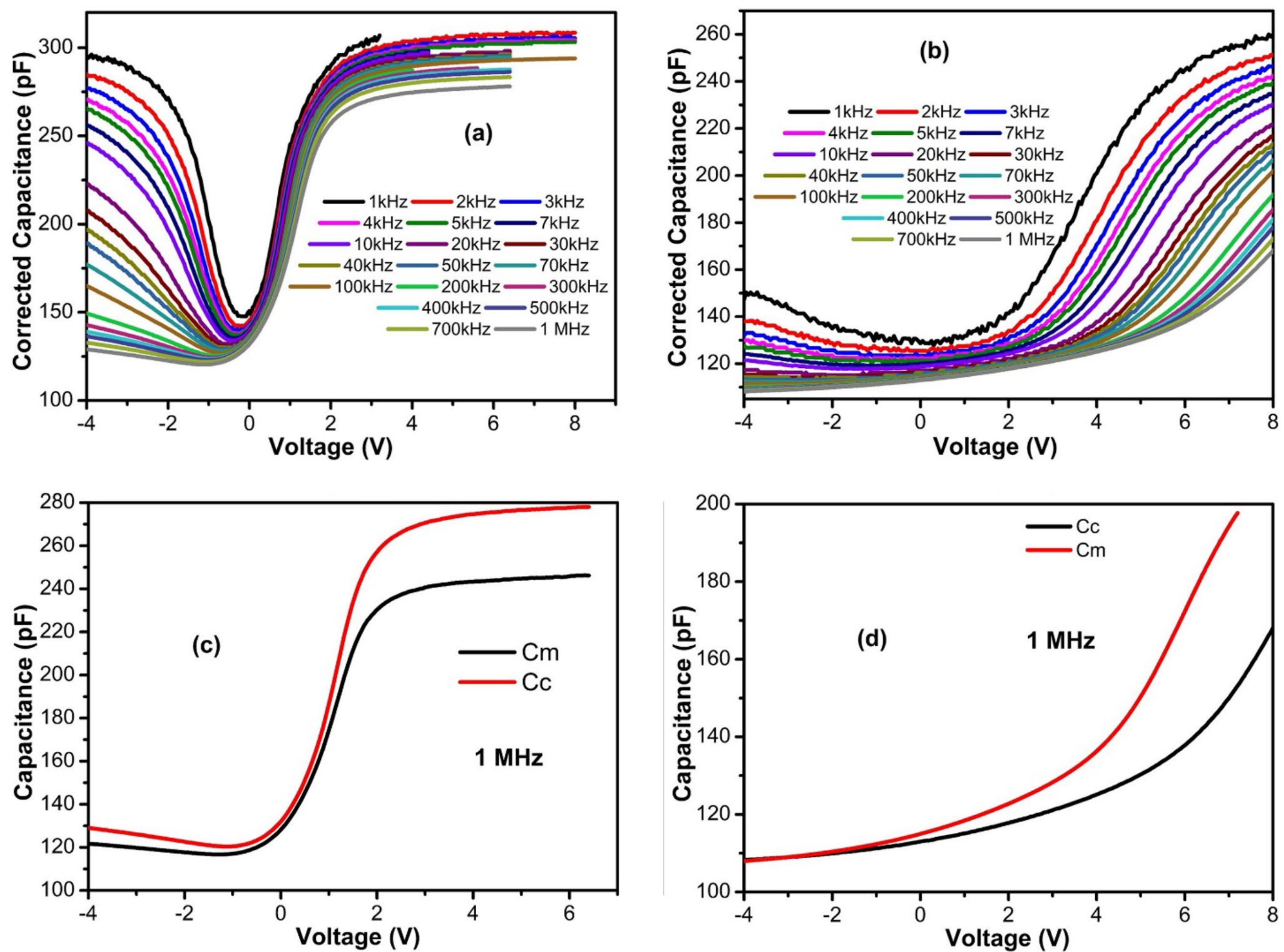

Fig. 10 Corrected capacitance plots of **a** undoped, **b** 10% Co-doped device. The comparison of measured and corrected capacitance plots of **c** undoped, **d** 10% Co-doped device at 1.0 MHz

respectively. The corrected capacitance surpasses the measured values, particularly in the accumulation region, for both devices.

For instance, in the case of the pure device, the corrected capacitance values are 308 pF at 2.0 kHz and 278 pF at 1.0 MHz, both measured at 6.0 V. In comparison, the measured values are slightly lower, standing at 307 pF at 2.0 kHz and 246 pF at 1.0 MHz, also at 6.0 V. Notably, the disparity between the capacitance values becomes more pronounced at higher frequencies. Similarly, for the 10% Co-doped device, the corrected capacitance values are 234 pF at 2.0 kHz and 138 pF at 1.0 MHz, recorded at 6.0 V, whereas the measured capacitance values for the same parameters are slightly higher, at 253 pF at 2.0 kHz and 173 pF at 1.0 MHz, also at 6.0 V. The corrected conductance (G_c) plots of both the pure and 10% Co-doped devices are showcased in Fig. 11. A noticeable distinction between the measured and corrected conductance plots is observed, indicative of the impact of series resistance and interface states on device characteristics. In the case of the pure device depicted in Fig. 11a, the measured conductance exhibits no peaks in the accumulation region, unlike the corrected conductance plots, which show a distinct peak in the same region. This discrepancy suggests that series resistance contributes to loss and obscures interface trap losses. Figures 11c and d illustrate the comparison of measured and corrected conductance plots at 1.0 MHz for the pure and 10% Co-doped devices, respectively. The marked differences in both plots underscore the influence of series resistance and interface effects on device parameters. Particularly in the accumulation region, the discrepancy between the measured and corrected

Fig. 11 Corrected conductance (G_c) plots for **a** pure and **b** 10% Co-doped device. The comparison corrected and measured the conductance of **c** pure and **d** 10% Co-doped device at 1.0 MHz

plots is most pronounced, emphasizing the dominant effect of series resistance in this region.

The Hill-Coleman method proves valuable in investigating the interface state density (N_{ss}) of the samples. This approach facilitates the calculation of N_{ss} through the following equation: [47]:

$$N_{ss} = \frac{2}{qA} \frac{\left(\frac{G_c}{\omega}\right)_{max}}{\left(\left(\frac{G_c}{\omega}\right)_{max} C_{ox}\right)^2 + \left(1 - \frac{C_c}{C_{ox}}\right)^2} \tag{15}$$

where the parameters were described before except for C_{ox}, which is oxide capacitance, and it is calculated using [31]:

$$C_{ox} = C_{ma}\left[1 + \left(\frac{G_{ma}}{\omega C_{ma}}\right)^2\right] \tag{16}$$

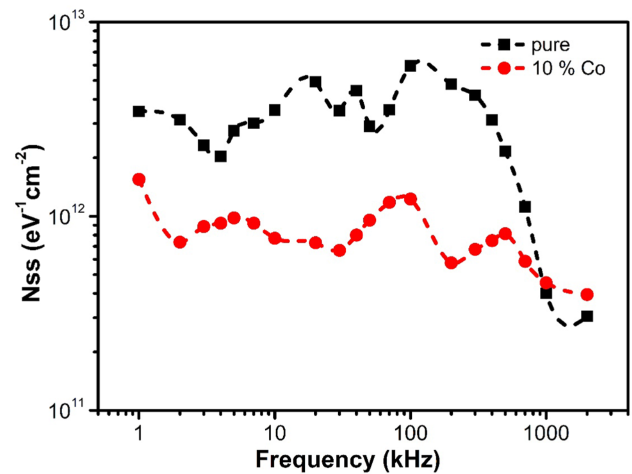

Fig. 12 The interface states variations depending on frequency for the pure and 10% Co-doped device

Figure 12 depicts the frequency-dependent distribution of N_{ss} for both the $YbFeO_3$/*p*-Si and Co-doped $YbFeO_3$/*p*-Si interfaces in each device. Notably, N_{ss} exhibits higher values in the low-frequency range and lower values in the high-frequency range. In the lower frequency range, N_{ss} can respond to the external electric field, thus contributing to the capacitance and conductance parameters. However, at higher frequencies, its ability to respond to the external electrical field diminishes, limiting its contribution to capacitance and conductance. The pure sample demonstrates a sharp decrease in N_{ss} after 200 kHz, whereas the doped sample shows a slower decrease after 400 kHz. It is evident from Fig. 12 that the pure sample exhibits higher interface state density than the Co-doped sample at each frequency. The 10% Co-doped $YbFeO_3$ thin film enhances the quality of the MS interface properties compared to the pure contact. Consequently, it can be inferred that interface state density can be reduced, and the semiconductor substrate surface can be modified by a thin 10% Co-doped $YbFeO_3$ interfacial layer between the MS contact.

Figure 13 illustrates the dependence of impedance on voltage for both the pure and doped devices across various frequency ranges. In the inversion region, impedance gradually increases as voltage approaches zero for both devices. It then peaks around zero volts in the depletion region, followed by a sharp decrease for positive voltages, and eventually stabilizes at higher voltages in the accumulation region for the undoped device in Fig. 13a. This decrease in impedance can be attributed to the increasing carrier mobility with increasing frequency. The observed peak may be due to interface states acting as trap sites that block carriers, resulting in increased resistance. The impedance values are measured at 5.1×10^5 Ω at 1.0 kHz and 594 Ω at 1.0 MHz, both at 7.0 V for the undoped device. The behavior of the 10% Co-doped device is similar, as shown in Fig. 13b, although the observed peak in the depletion region is not as prominent as in the undoped device. Additionally, the doping process leads to an increase in impedance compared to the undoped device, with impedance values measured at 6.1×10^5 Ω at 1.0 kHz and 819 Ω at 1.0 MHz, both at 7.0 V for the 10% Co-doped device. The insets display the suppressed impedance plots, which are not visible in the main figures.

4 Conclusion

Thin films of pure $YbFeO_3$ and 10% Co-doped $YbFeO_3$ were deposited onto *p*-Si substrates using the rf magnetron sputtering technique, maintaining a substrate temperature of 500 °C throughout the deposition process. SEM analysis revealed that pure $YbFeO_3$ exhibited a spongy/porous structure, while the 10% Co-doped $YbFeO_3$ displayed a dense and crack-free surface. Electrical characterization was conducted at room temperature (300 K) under ambient conditions. The capacitance–voltage and conductance-voltage characteristics were measured across various frequencies within the voltage range of − 4 V to 8 V.

The capacitance gradually decreased from low to high-frequency values. Specifically, in the accumulation region, the capacitance was measured at 313 pF

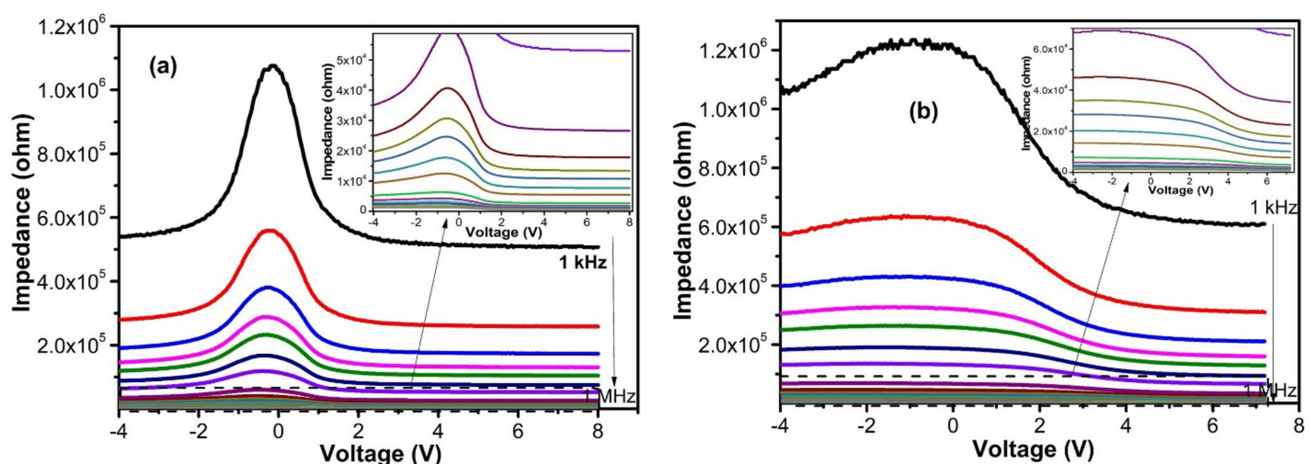

Fig. 13 Impedance (*Z*) variations of the **a** pure and **b** 10% Co-doped $YbFeO_3$ devices

at 1.0 kHz and 247 pF at 1.0 MHz for pure $YbFeO_3$, and 263 pF at 1.0 kHz and 195 pF at 1.0 MHz for 10% Co-doped $YbFeO_3$, both at 7.0 V. G–V measurements indicated that increased frequency led to increased conductivity due to enhanced charge mobility. Conductance values were determined as 1.03×10^{-7} S at 1.0 kHz, 5.55×10^{-4} S at 1.0 MHz, 8.03×10^{-8} S at 1.0 kHz, and 2.11×10^{-4} S at 1.0 MHz at 7.0 V in the accumulation region.

Parameters such as free carrier density, diffusion potential, barrier height, energy difference between the bulk Fermi level and valence band edge, image force barrier lowering, and maximum electrical field were obtained using C^{-2}–V plots. Voltage and frequency-dependent series resistance were determined using C–V and G–V measurements. In the accumulation region, resistance values were approximately 11.3 kΩ at 2.0 kHz and 211 Ω at 1.0 MHz for undoped devices, and 29.7 kΩ at 2.0 kHz and 158.6 Ω at 1.0 MHz for 10% Co-doped samples, both at 7.0 V.

Impedance measurements revealed a relaxation peak attributable to the existence of interface states, with impedance values of 5.1 × 105 Ω at 1.0 kHz and 594 Ω at 1.0 MHz for the undoped device, and 6.1 × 105 Ω at 1.0 kHz and 819 Ω at 1.0 MHz for the 10% Co-doped device, both at 7.0 V. Corrected capacitance and conductance results underscored the significant role of series resistance in the electrical parameters of semiconductor materials. Additionally, interface state density was determined using the Hill-Coleman relation, highlighting its prevalence in the low-frequency region. The 10% Co-doped $YbFeO_3$ thin film was observed to enhance the quality of the MS interface properties compared to the pure contact, suggesting that interface state density can be reduced, and the semiconductor substrate surface modified by a thin 10% Co-doped $YbFeO_3$ interfacial layer between MS contacts.

Acknowledgements

This work was supported by The Scientific and Technological Research Council of Türkiye (TUBITAK) through Grant No: 116F025. We acknowledge Istanbul Medeniyet University Science and Advanced Technology Research Center (IMU-BILTAM). We acknowledge CzechNanoLab Research Infrastructure supported by MEYS CR (LM2023051).

Author contributions

MC contributed to conceptualization, investigation, validation, and writing of the original draft. OP contributed to investigation, validation, editing of the original draft, funding acquisition, and supervision. IO contributed to investigation and validation. FMC contributed to investigation and validation. YY contributed to investigation and validation. DS contributed to investigation and validation. CS contributed to investigation and validation. ZD contributed to investigation and validation. YC contributed to investigation and validation. MC contributed to investigation and validation. AT contributed to investigation, validation, editing of the original draft, and supervision.

Funding

Open access funding provided by the Scientific and Technological Research Council of Türkiye (TÜBİTAK). Funding was supported by Türkiye Bilimsel ve Teknolojik Araştırma Kurumu, 116F025.

Data availability

All the necessary Data are available within the main text.

Declarations

Competing interests The author declare that they have no known competing financial interests or personal relationships that could have appeared to influence the work reported in this paper.

Supplementary Information The online version contains supplementary material available at https://doi.org/10.1007/s10854-024-12896-8.

Open Access This article is licensed under a Creative Commons Attribution 4.0 International License, which permits use, sharing, adaptation, distribution and reproduction in any medium or format, as long as you give appropriate credit to the original author(s) and the source, provide a link to the Creative Commons licence, and indicate if changes were made. The images or other third party material in this ar-

ticle are included in the article's Creative Commons licence, unless indicated otherwise in a credit line to the material. If material is not included in the article's Creative Commons licence and your intended use is not permitted by statutory regulation or exceeds the permitted use, you will need to obtain permission directly from the copyright holder. To view a copy of this licence, visit http://creativecommons.org/licenses/by/4.0/.

References

1. B.-O. Cho, J. Wang, L. Sha, J.P. Chang, Tuning the electrical properties of zirconium oxide thin films. Appl. Phys. Lett. **80**, 1052 (2002)
2. C.-K. Min, T.-B. Wu, W.-T. Yang, C.-L. Chen, Functionalized mesoporous silica/polyimide nanocomposite thin films with improved mechanical properties and low dielectric constant. Compos. Sci. Technol. **68**, 1570–1578 (2008)
3. T. Liang, Y. Makita, S. Kimura, Effect of film thickness on the electrical properties of polyimide thin films. Polymer **42**, 4867–4872 (2001)
4. F.M. Pontes, E.J.H. Lee, E.R. Leite, E. Longo, J.A. Varela, High dielectric constant of $SrTiO_3$ thin films prepared by chemical process. J. Mater. Sci. **35**, 4783–4787 (2000)
5. H. Kacus, M. Yilmaz, A. Kocyigit, U. Incekara, S. Aydogan, Optoelectronic properties of Co/pentacene/Si MIS heterojunction photodiode. Physica B **597**, 412408 (2020)
6. C. Sasikala, G. Suresh, N. Durairaj, I. Baskaran, B. Sathyaseelan, M. Kumar, K. Senthilnathan, E. Manikandan, Influences of Ti4þ ion on dielectric property in perovskite structure of La ferrite ($LaFe_{1-X}Ti_XO_3$). J. Alloy. Compd. **845**, 155040 (2020)
7. Z.J. Corey, P. Lu, G. Zhang, Y. Sharma, B.X. Rutherford, S. Dhole, P. Roy, Z. Wang, Y. Wu, H. Wang, A. Chen, Q. Jia, Structural and optical properties of high entropy (La, Lu, Y, Gd, Ce)AlO_3 perovskite thin films. Adv. Sci. **9**, 2202671 (2022)
8. H. Akamatsu, K. Fujita, H. Hayashi, T. Kawamoto, Y. Kumagai, Y. Zong, K. Iwata, F. Oba, I. Tanaka, K. Tanaka, Crystal and electronic structure and magnetic properties of divalent europium perovskite oxides $EuMO_3$ (M = Ti, Zr, and Hf): experimental and first-principles approaches. Inorg. Chem. **51**, 4560–4567 (2012)
9. Z. Zhou, L. Guo, H. Yang, Q. Liu, F. Ye, Hydrothermal synthesis and magnetic properties of multiferroic rare-earth orthoferrites. J. Alloy. Compd. **583**, 21–31 (2014)
10. K. Lee, S. Hajra, M. Sahu, H.J. Kim, Colossal dielectric response, multiferroic properties, and gas sensing characteristics of the rare earth orthoferrite $LaFeO_3$ ceramics. J. Alloy. Compd. **882**, 160634 (2021)
11. A. Anantharaman, T.L. Ajeesha, J.N. Baby, M. George, Effect of structural, electrical and magneto-optical properties of $CeMn_xFe_{1-x}O_{3-\delta}$ perovskite materials. Solid State Sci. **99**, 105846 (2020)
12. O. Polat, M. Caglar, F.M. Coskun, M. Coskun, Y. Caglarc, A. Turut, An experimental investigation: the impact of cobalt doping on optical properties of $YbFeO_{3-\delta}$ thin film. Mater. Res. Bull. **119**, 110567 (2019)
13. O. Polat, M. Coskun, F.M. Coskun, B. Zengin Kurt, Z. Durmus, Y. Caglar, M. Caglar, A. Turut, Electrical characterization of Ir doped rare-earth orthoferrite $YbFeO_3$. J. Alloys Compd. **787**, 1212–1224 (2019)
14. R.C. Rai, C. Horvatits, D. Mckenna, J. Du Hart, Structural studies and physical properties of hexagonal-$YbFeO_3$ thin films. AIP Adv. **9**, 015019 (2019)
15. H. Han, D. Kim, K. Chu, J. Park, S.Y. Nam, S. Heo, C.-H. Yang, H.M. Jang, Enhanced switchable ferroelectric photovoltaic effects in hexagonal ferrite thin films via strain engineering. ACS Appl. Mater. Interfaces **10**, 1846–1853 (2018)
16. X. Li, Y. Yun, A.S. Thind, Y. Yin, Q. Li, W. Wang, A.T. N'Diaye, C. Mellinger, X. Jiang, R. Mishra, X. Xu, Domain-wall magnetoelectric coupling in multiferroic hexagonal $YbFeO_3$ films. Sci. Rep. **13**, 1755 (2023)
17. F. Meng, J. Hu, C. Liu, Y. Tan, Y. Zhang, Highly sensitive and low detection limit of acetone gas sensor based on porous $YbFeO_3$ nanocrystallines. Chem. Phys. Lett. **780**, 138925 (2021)
18. P. Zhang, H. Qin, W. Lv, H. Zhang, J. Hu, Gas sensors based on ytterbium ferrites nanocrystalline powders for detecting acetone with low concentrations. Sens. Actuators B **246**, 9–19 (2017)
19. S. Tikhanova, A. Seroglazova, M. Chebanenko, V. Nevedomskiy, V. Popkov, Effect of TiO_2 additives on the stabilization of h-$YbFeO_3$ and promotion of photo-fenton activity of o-$YbFeO_3$/h-$YbFeO_3$/r-TiO_2 nanocomposites. Materials **15**, 8273 (2022)
20. H. Iida, T. Koizumi, Y. Uesu, K. Kohn, N. Ikeda, S. Mori, R. Haumont, P.-E. Janolin, J.-M. Kiat, M. Fukunaga, Y. Noda, Ferroelectricity and ferrimagnetism of hexagonal $YbFeO_3$ thin films. J. Phys. Soc. Jpn. **81**, 024719 (2012)
21. O. Polat, M. Caglar, F.M. Coskun, M. Coskun, Y. Caglar, A. Turut, An investigation of the optical properties of $YbFe_{1-x}Ir_xO_{3-\delta}$ (x= 0, 0.01 and 0.10) orthoferrite films. Vacuum **173**, 109124 (2020)

22. O. Polat, M. Caglar, F.M. Coskun, D. Sobola, M. Konecný, M. Coskun, Y. Caglar, A. Turut, Examination of optical properties of $YbFeO_3$ films via doping transition element osmium. Opt. Mater. **105**, 109911 (2020)
23. O. Polat, M. Coskun, H. Efeoglu, M. Caglar, F.M. Coskun, Y. Caglar, A. Turut, The temperature induced current transport characteristics in the orthoferrite $YbFeO_{3-\delta}$ thin film/p-type Si structure. J. Phys.: Condens. Matter. **33**, 035704 (2021)
24. Z. Berktaş, E. Orhan, M. Ulusoy, M. Yildiz, Ş Altındal, Negative capacitance behavior at low frequencies of nitrogen doped polyethylenimine-functionalized graphene quantum dotsbased structure. ACS Appl. Electron. Mater. **5**(3), 1804–1811 (2023)
25. H.G. Çetinkaya, M. Yıldırım, P. Durmus, S. Altındal, Diode-to-diode variation in dielectric parameters of identically prepared metal-ferroelectric-semiconductor structures. J. Alloy. Compd. **728**, 896–901 (2017)
26. I. Orak, A. Kocyigit, A. Turut, The surface morphology properties and respond illumination impact of ZnO/n-Si photodiode by prepared atomic layer deposition technique. J. Alloy. Compd. **691**, 873–879 (2017)
27. Ö. Vural, Y. Safak, A. Türüt, S. Altındal, Temperature dependent negative capacitance behavior of Al/rhodamine-101/n-GaAs Schottky barrier diodes and Rs effects on the C-V and G/ω–V characteristics. J. Alloy. Compd. **513**, 107–111 (2012)
28. Ö. Güllü, A. Türüt, n -type InP Schottky diodes with organic thin layer: Electrical and interfacial properties. J. Vac. Sci. Technol., B **28**, 466 (2010)
29. M. Caglar, S. Ilican, Y. Caglar, F. Yakuphanoglu, Electrical conductivity and optical properties of ZnO nanostructured thin film. Appl. Surf. Sci. **255**, 4491–4496 (2009)
30. N.A. Al-Ahmadi, Metal oxide semiconductor-based Schottky diodes: a review of recent advances. Mater. Res. Express **7**, 032001 (2020)
31. E.H. Nicollian, J.R. Brews, *MOS (metal oxide semiconductor) Physics AND technology* (John Wiley & Sons, New York, 1982)
32. Ö. Vural, Y. Şafak, Ş Altındal, A. Türüt, Current–voltage characteristics of Al/Rhodamine-101/n-GaAs structures in the wide temperature range. Curr. Appl. Phys. **10**(3), 761–765 (2010)
33. M.T. Güneser, H. Elamen, Y. Badali, S. Altındal, Frequency dependent electrical and dielectric properties of the Au/(RuO_2: PVC)/n-Si (MPS) structures. Physica B **657**, 414791 (2023)
34. A. Barkhordari, H. Mashayekhi, P. Amiri, Ş Altındal, Y.A. Kalandaragh, On the investigation of frequency-dependent dielectric features in Schottky barrier diodes (SBDs) with polymer interfacial layer doped by graphene and $ZnTiO_3$ nanostructures. Appl. Phys. A **129**, 249 (2023)
35. O. Polat, M. Coskun, F.M. Coskun, J. Zlamal, B. Zengin Kurt, Z. Durmus, M. Caglar, A. Turut, Co doped $YbFeO_3$: exploring the electrical properties via tuning the doping level. Ionics **25**, 4013–4029 (2019)
36. E.A. Nforna, P.K. Tsobnang, R.L. Fomekong, H.M.K. Tedjieukeng, J.N. Lambi, J.N. Ghogomu, Effect of B-site Co substitution on the structure and magnetic properties of nanocrystalline neodymium orthoferrite synthesized by auto-combustion. R. Soc. Open Sci. **7**, 201883 (2021)
37. L. Bai, M. Sun, W. Ma, J. Yang, J. Zhang, Y. Liu, Enhanced magnetic properties of co-doped $BiFeO_3$ thin films via structural progression. Nanomaterials **10**, 1798 (2020)
38. T.-M. Pan, Y.-S. Huang, J.-L. Her, Sensing and impedance characteristics of $YbTaO_4$ sensing membranes. Sci. Rep. **8**, 12902 (2018)
39. N.M. Vuong, N.D. Chinh, B.T. Huy, Y.-I. Lee, CuO-decorated ZnO hierarchical nanostructures as efficient and established sensing materials for H_2S gas sensors. Sci. Rep. **6**, 26736 (2016)
40. L. Jing, B. Xin, F. Yuan, L. Xue, B. Wang, H. Fu, Effects of surface oxygen vacancies on photophysical and photochemical processes of Zn-doped TiO_2 nanoparticles and their relationships. J. Phys. Chem. B **110**, 17860–17865 (2006)
41. P.S.J. Bharadwaj, S. Kundu, V.S. Kollipara, K.B.R. Varma, Synergistic effect of trivalent (Gd^{3+}, Sm^{3+}) and highvalent (Ti^{4+}) co-doping on antiferromagnetic $YFeO_3$. RSC Adv. **10**, 22183 (2020)
42. S. Gupta, R. Medwal, S.P. Pavunny, D. Sanchez, R.S. Katiyar, Temperature dependent Raman scattering and electronic transitions in rare earth $SmFeO_3$. Ceram. Int. **44**, 4198–4203 (2018)
43. O. Rejaiba, A.F.B. de Cal, A. Matoussi, A comprehensive study on the interface states in the ECR-PECVD SiO_2/p-Si MOS structures analyzed by different method. Physica E **109**, 84–92 (2019)
44. L.J. Downie, R.J. Goff, W. Kockelmann, S.D. Forder, J.E. Parker, F.D. Morrison, P. Lightfoot, Structural, magnetic and electrical properties of the hexagonal ferrites MFeO3 (M=Y, Yb, In). J. Solid State Chem. **190**, 52–60 (2012)
45. A. Mutale, S.C. Deevi, E. Yilmaz, Effect of annealing temperature on the electrical characteristics of Al/Er_2O_3/n-Si/Al MOS capacitors. J. Alloy. Compd. **863**, 158718 (2021)
46. A. Tataroglu, S. Altındal, M.M. Bulbul, Temperature and frequency dependent electrical and dielectric properties of Al/SiO_2/p-Si (MOS) structure. Microelectron. Eng. **81**, 140–149 (2005)

47. W.A. Hill, C.C. Coleman, A single-frequency approximation for interface-state density determination. Solid-State Electron. **23**, 987–993 (1980)

Publisher's Note Springer Nature remains neutral with regard to jurisdictional claims in published maps and institutional affiliations.